

$\text{Sn}_{1-x}\text{Ge}_x\text{O}_y$ and $\text{Zn}_{1-x}\text{Ge}_x\text{O}_y$ by Atomic Layer Deposition—Growth Dynamics, Film Properties, and Compositional Tuning for Charge Selective Transport in $(\text{Ag},\text{Cu})(\text{In},\text{Ga})\text{Se}_2$ Solar Cells

Adam Hultqvist,* Jan Keller, Natalia M. Martin, Fredrik Larsson, and Tobias Törndahl



Cite This: ACS Appl. Energy Mater. 2023, 6, 9824–9836



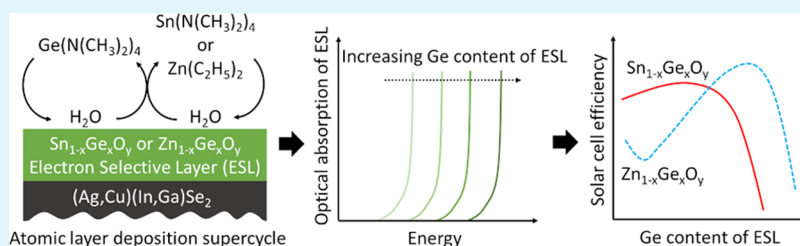
Read Online

ACCESS |

Metrics & More

Article Recommendations

Supporting Information



ABSTRACT: Two inorganic electron-selective layers (ESLs), $\text{Sn}_{1-x}\text{Ge}_x\text{O}_y$ (TGO) and $\text{Zn}_{1-x}\text{Ge}_x\text{O}_y$ (ZGO), were developed by using atomic layer deposition (ALD) with in situ quartz crystal monitoring. To ensure $(\text{Ag},\text{Cu})(\text{In},\text{Ga})\text{Se}_2$ (ACIGS) solar cell compatibility, a 120 °C ALD process was developed for GeO_y using $\text{Ge}(\text{N}(\text{CH}_3)_2)_4$ and H_2O as precursors. In the ALD supercycle approach, the GeO_y ALD cycle was interchanged with either ZnO or SnO_y cycles to deposit TGO and ZGO with varying conduction band positions (E_c), respectively. The material properties were experimentally verified using X-ray photoelectron spectroscopy and optical absorption and by employing these films as ESLs in ACIGS solar cells. There, the open-circuit voltage initially increased as the Ge content of the TGO and ZGO films increased due to the ESL E_c simultaneously shifting up from the low position in ZnO or SnO_y to match the ACIGS E_c . As the Ge content increased further, the fill factor (FF) of these devices decreased since the ESL E_c became positioned significantly above the ACIGS E_c , forming an energy barrier as seen from ACIGS. As a result, the efficiency of the ACIGS solar cell peaked for an intermediate Ge content for both TGO and ZGO. Using good TGO and ZGO compositions in ACIGS solar cells gave efficiencies of up to 14.8 and 17.0%, respectively, which were lower than the reference best cell efficiencies of up to 19.5% for CdS and 18.2% for $\text{Zn}_{1-x}\text{Sn}_x\text{O}_y$ (ZTO). ZGO was, however, able to shift its E_c further up than ZTO, making it a potent ESL for high-band-gap absorbers. Based on the results, we listed a few key properties that are required for a good ACIGS solar cell ESL and gave a few suggestions on how they are linked to the previous success of ZTO.

KEYWORDS: electron transport layer, buffer layer, $(\text{Ag},\text{Cu})(\text{In},\text{Ga})\text{Se}_2$, atomic layer deposition, photovoltaics

INTRODUCTION

Recently, atomic layer deposition (ALD) has been a vital tool for enabling the further development of monolithically integrated circuits.¹ Some key aspects of the deposition technique have been the conformal growth, the excellent thickness control, the possibility to create distinct interfaces, and the low deposition temperatures.²

These aspects have also been interesting for other ALD applications, such as solar cells. For mass-produced silicon solar cells, it has been crucial to make thin, conformal insulating films that electrically passivate contact surfaces.³ For the up-and-coming perovskite technologies, the conformality and the low deposition temperature that ALD enables have been used to create high-quality, transparent, and charge selective layers without damaging the perovskite beneath and, at the same time, preventing degradation through ion movement within the stack.^{4,5} Similarly, transparent electron-selective layers (ESLs) have also been grown directly on

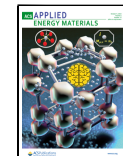
$\text{Cu}_2\text{ZnSn}(\text{S},\text{Se})_4$ (CZTS), $(\text{Ag},\text{Cu})(\text{In},\text{Ga})\text{Se}_2$ (ACIGS), and SnS solar cell absorbers with excellent results due to the conformality, low deposition temperature, and low surface damage of the ALD process.^{6–8}

In addition, some of the studies on ACIGS utilized another ALD aspect, namely, the ability to accurately tune the composition of a material and thereby its properties. In these cases, a certain placement of the energy conduction band level (E_c) in the ESL was desired for optimal charge extraction from the ACIGS absorber and minimized interface recombination. In general, the studies first identified ALD processes for two

Received: April 14, 2023

Accepted: August 30, 2023

Published: September 22, 2023



binary compounds with significant differences in the E_c placement. Then, an ALD supercycle was employed where cycles from the two binary processes were mixed with the idea that the resulting ternary compound had an E_c placement that depended on the mixing ratio. By varying the mixing ratio of the supercycle, optimal ESL E_c placements for the solar cell performance were identified for each of the ternary compounds Zn(O,S),⁹ (Zn,Mg)O,¹⁰ Zn_{1-x}Sn_xO_y (ZTO),¹¹ ZnIn_xS_y,¹² ZnTiO,¹³ SnGaO_x (TGAO),¹⁴ and In₂(S,O)₃.¹⁵

In comparison to the common low-Ag content (10–20%) and low-Ga content (20–30%) ACIGS, several of the more recently emerging solar cell absorbers, such as halide perovskites, kesterites, or higher-band-gap chalcopyrites, have higher E_c placements.^{16,17} Initial results show that especially ZTO can clearly improve the open-circuit voltage (V_{oc}) of these devices by shifting its E_c up.^{18–21} However, since the E_c shift is limited in ZTO, it cannot match most of these absorbers' E_c fully; therefore, there is still room to further improve V_{oc} by shifting the ESL E_c further up.²² Thus, there has been a need to find other ESL options with this possibility.

With that in mind, we set out to make ESL compounds with high and adjustable E_c through an ALD supercycle scheme by first selecting GeO_y due to its high E_c placement and 4–6 eV energy band gap (E_g).^{23,24} In order to adjust the E_c of the resulting ternary compound, we mixed the GeO_y process with either the ZnO or SnO_y process, both having lower E_c placements.^{22,24} Ideally, the resulting ternary Zn_{1-x}Ge_xO_y (ZGO) and Sn_{1-x}Ge_xO_y (TGO) compounds should have E_c positions that shift to higher energies as the Ge content of the compounds increases (Figure 1). Recently, this was shown for

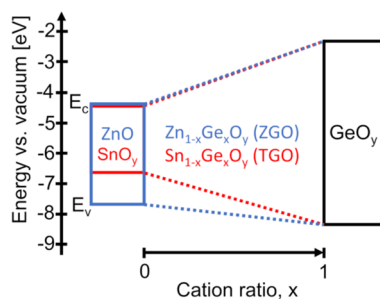


Figure 1. Estimated range of E_c and E_v positions as a function of the cation ratio in ZGO (blue) and TGO (red) films based on previous findings for the E_c and E_v positions of ZnO, SnO_y, and GeO_y.^{21–23}

TGO and ZGO ESLs grown at a high temperature, 200 °C, by ALD and chemical vapor deposition (CVD), respectively. When applied as ESLs in SnS and Cu(In,Ga)Se₂ (CIGS) solar cells, respectively, the preliminary data showed that the device performance was indeed affected by the Ge content.^{8,25} To further investigate whether ZGO and TGO have the intended E_c trends and therefore can work as ESLs for temperature-sensitive absorbers such as ACIGS²⁶ and perovskite,²⁷ low-temperature (120 °C) ALD processes, using different precursors, were developed for GeO_y. ZGO and TGO were studied using in situ quartz crystal microbalance (QCM) monitoring. ZGO and TGO with varying Ge content films were also deposited on fused silica, and their morphological, compositional, optical, and electrical properties were analyzed by X-ray diffraction (XRD), X-ray fluorescence (XRF), X-ray reflectivity (XRR), X-ray photoelectron spectroscopy (XPS), four-point probing (4PP), scanning electron microscopy

(SEM), optical reflectance, and optical transmittance. The TGO and ZGO films were also used as ESLs in ACIGS solar cells to evaluate their ESL performance and their ability to match the absorber E_c by changing their Ge content. ACIGS absorbers were well suited for this initial ESL testing since the resulting solar cell performance is sensitive to the ESL E_c position and the absorber can be uniformly deposited over large areas. Additionally, TGO and ZGO were directly compared to ZTO, where all ESLs had similar E_c positions, explaining why the ZTO ESL usually showed good solar cell device performance. The results showed that the ALD ZGO and TGO compounds developed in this study are two very interesting ESL candidates for solar cell absorbers with high E_c positions and provided insight into why previously developed Zn-containing ESLs such as ZTO have worked so well for ACIGS solar cells.

EXPERIMENTAL SECTION

Atomic Layer Deposition and In Situ Analysis Using a Quartz Crystal Microbalance. The SnO_y, ZnO, GeO_y, ZGO, and TGO films were deposited using thermally activated ALD at a temperature of 120 or 150 °C in a Microchemistry F120 viscous flow reactor using N₂ carrier gas (99.9999%). Zn precursor Zn(C₂H₅)₂ (diethylzinc, DEZ, AkzoNobel TCO grade) and O precursor H₂O (deionized water, 18 MΩ cm) were effused into the reactor. Sn precursor Sn(N(CH₃)₂)₄ (tetrakisdimethylamino-tin, TDMASn, SAFC research grade) and Ge precursor Ge(N(CH₃)₂)₄ (tetrakisdimethylamino-germanium, TDMAGe, Pegasus) were heated to 40 and 45 °C, respectively, in bubblers that use N₂ to carry the precursor into the reactor. An ALD cycle of TDMAGe-pulse/N₂-purge/H₂O-pulse/N₂-purge was used to grow the GeO_y film. The two ternary compounds ZGO and TGO were grown using ALD supercycle schemes where the previously described GeO_y cycle was alternated with either the ZnO cycle, DEZ pulse/N₂-purge/H₂O-pulse/N₂-purge or the SnO_y cycle, TDMASn-pulse/N₂-purge/H₂O-pulse/N₂-purge. For all of these processes, the pulse and purge times were between 0.5 and 16 s; see the Supporting Information (SI) for further details.

The QCM holder was custom-made for the F120 Microchemistry reactor to place the active QCM surface in the normal substrate position. Unpolished and AT cut QCM crystals optimized for 120 °C were used (Inficon 750-1058-G10). The QCM signal was sent to an Inficon SQM 160 thin-film deposition monitor, where time vs frequency output was recorded. The frequency shift was used to estimate the mass change per area through the Sauerbrey equation (eq 1), where f_0 is the fundamental crystal resonance frequency, A is the active crystal resonator area, μ_0 is the density of quartz, and ρ_0 is the shear modulus of quartz.^{28,29} The specific mass gain per cycle (MPC) was calculated using a previously developed MATLAB script.³⁰

$$\Delta f = -\frac{2f_0^2}{A\sqrt{\rho_0\mu_0}} \Delta m \quad (1)$$

Ex Situ Analysis. To investigate the material properties, 30–70 nm thick GeO_y, ZGO, and TGO films were deposited on fused silica (Table S1). At the same time, ACIGS absorbers were also included in the chamber to evaluate the films as ESLs in the ZnO:Al/ZnO/ESL/ACIGS/Mo/soda lime glass (SLG) solar cell stack.

The cation ratios $[Ge]/([Ge] + [Zn])$ and $[Ge]/([Ge] + [Sn])$ of the films were determined by XRF (PANalytical Epsilon 5), where the signals from the Zn $K\alpha$, Ge $K\alpha$, and Sn $K\alpha$ peaks were collected and background-corrected for films grown on fused silica substrates. A SrF₂ secondary target was used for Zn $K\alpha$ and Ge $K\alpha$, whereas a BaF₂ secondary target was used for Sn $K\alpha$. All XRF cation ratios were calibrated to Rutherford backscattering (RBS) measurements for the ZGO 0.26 and TGO 0.3 samples.

To maximize the signal from the films, an angle of incidence of 0.3° , i.e., close to the critical angle, was used for XRD (GI-XRD). The system (Philips X'Pert MRD) used Cu $K\alpha$ radiation with an X-ray mirror on the primary side and a 0.27° parallel plate collimator on the detector side. The same system was used for XRR, except that the optics was changed to also use a matching divergence slit on the primary side and a 0.09° parallel plate collimator on the detector side. The XRR curves were fitted with the X'Pert reflectivity program.

Transmittance and reflectance data for the films were measured using a spectrophotometer (Lambda 900, PerkinElmer) equipped with an integrating sphere. The absorption coefficient was calculated from the measured transmittance and reflectance and the film thickness measured by XRR.³¹

Sheet resistance (R_{\square}) for the films was measured by a 4PP instrument (CMT-SR2000N, Advanced Instrument Technology). Using R_{\square} and the thickness, t_{film} , determined from XRR, the film resistivity, ρ , was estimated from $\rho = R_{\square} t_{film}$.

XPS measurements were carried out by employing a PHI Quantera II scanning XPS microprobe with monochromated Al $K\alpha$ (1486.6 eV) and a beam diameter of $100 \mu\text{m}$. A pass energy of 55 eV with dwell times of 0.05 s point was used to collect the valence band spectra. The samples were exposed to air during sample transfer and had a small carbon surface contamination observed on all samples. To minimize charging during measurements, charge neutralization has been employed, which led to very similar core level peak positions for an individual sample after ~ 40 min of measurement time.

Microstructural imaging was performed by SEM employing Zeiss LEO 1550 and Zeiss LEO 1530 microscopes using 3 keV acceleration voltage, $10 \mu\text{A}$ current, and an in-lens detector.

Fabrication and Analysis of Solar Cells. The solar cell devices used a ZnO:Al/ZnO/ESL/ACIGS/Mo/SLG stack and had a total area of 0.05 cm^2 . An SEM micrograph of the full solar cell stack can be found in the SI (Figure S1). Both the sputtered Mo and the coevaporated ACIGS were deposited at Solibro Research AB. For the ZGO series, the ACIGS was left as deposited before storage, whereas it underwent an RbF postdeposition treatment and received a 21 nm CdS capping layer prior to storage for the TGO and comparison series. For the ZGO and TGO series, the ACIGS compositions were determined by XRF to be $(\text{Ag} + \text{Cu})/(\text{In} + \text{Ga}) = 0.86$ and 0.84 , $\text{Ga}/(\text{In} + \text{Ga}) = 0.28$ and 0.27 , and $\text{Ag}/(\text{Ag} + \text{Cu}) = 0.19$ and 0.19 . The ACIGS film thicknesses were $2.2 \mu\text{m}$ in both cases. Right before the ALD deposition, the ACIGS was taken out of storage and etched for 1 min in HCl (2 M) to clean the surface and to remove the RbF/CdS capping stack present on it for the TGO series.³² For reference, 50 nm CdS was also deposited on one of the samples of each series instead of the ALD film by using an established chemical bath process (CBD).³³ The ZnO:Al/ZnO stack was radio frequency (RF)-sputtered onto the ESL following an established process.³³ Finally, the cells were defined by using mechanical scribing of the ZnO:Al/ZnO/ESL/ACIGS substack. As a result, all cells

shared the Mo film as their bottom contact but had individual ZnO:Al top contacts.

Current density–voltage ($J-V$) measurements were performed using scans, which went from negative to positive bias with a speed of 400 mV/s and a step size of 5 mV. In the setup, the substrates were kept at 25°C using a Peltier element. A halogen lamp (FHS 300W 82 V GX 5.3, Osram) calibrated to give the same current density as the air mass (AM) 1.5 spectrum for a Si-reference cell (Hamamatsu S1337-66BR, Hamamatsu Photonics K.K.) was used as the light source. External quantum efficiency (EQE) was measured by a home-built system using a Xe lamp, a monochromator, a signal chopper for the light path to the cell, and a lock-in amplifier for the electric signal readout from the solar cell.

RESULTS AND DISCUSSION

ALD Growth Dynamics. The GeO_y ALD process was developed at a deposition temperature of 120°C to make it compatible with the previously established SnO_y and ZnO processes and with ACIGS-based solar cells.^{11,34} From analyzing QCM data, see the SI for further details, the pulse and purge times of the GeO_y ALD cycle, TDMA Ge/N_2 -purge/ $\text{H}_2\text{O}/\text{N}_2$ -purge, were chosen to be $1/2/4/4$ s, respectively. While not giving a fully saturated reaction, the H_2O pulse length was chosen to be 4 s as a tradeoff between the reaction fully saturating and the processing time (Figure S2a). To ensure a uniform coating over the entire $5 \times 5 \text{ cm}^2$ deposition zone, the N_2 -purge times were also set to be 2 and 4 s following the TDMA Ge and H_2O pulses, respectively, rather than 1 s, which the centrally placed QCM suggested to be long enough.

The GeO_y process was interchanged with a previously established SnO_y process¹¹ through an ALD supercycle scheme to create a TGO deposition process. The pulse and purge dynamics were analyzed using QCM and a Ge/(Ge + Sn) pulse ratio of 0.5 or alternating every other SnO_y subcycle with a GeO_y subcycle (Figure S2b). Based on this, pulse and purge times of $1/2/1/2:1/2/1/2$ s were chosen for the SnO_y subcycle, TDMA Sn/N_2 -purge/ $\text{H}_2\text{O}/\text{N}_2$ -purge:TDMA Ge/N_2 -purge/ $\text{H}_2\text{O}/\text{N}_2$ -purge, and the GeO_y subcycle, TDMA Ge/N_2 -purge/ $\text{H}_2\text{O}/\text{N}_2$ -purge, respectively (see the SI for further details). Figure 2a and Table 1 show that the measured RBS/XRF $[Ge]/([Ge] + [Sn])$ cation ratio, x -value, for TGO films on fused silica is just a bit lower than the ALD Ge/(Ge + Sn) pulse ratio. The measured growth per cycle (GPC) for these films decreases as the pulse ratio increases (Figure 2b and Table S2). This trend appears almost as a linear combination of the lower GPC GeO_y subcycle and the larger GPC SnO_y subcycle. Both the trend in the cation ratio and the trend in GPC are also supported by QCM data (see the SI for details) and suggest that the SnO_y and GeO_y subcycles affect each other only to a minor extent. This results in an easy and predictable ALD process for TGO.

The ZGO processes used a similar supercycle scheme to TGO, where ZnO subcycles from a previously established process³⁴ were interchanged with GeO_y subcycles. By alternating every ZnO subcycle with a GeO_y subcycle, using a Ge/(Ge + Zn) pulse ratio of 0.5, the pulse and purge times were investigated and chosen to be $1/2/1/4$ and $1/2/1/4$ s for the ZnO subcycle, DEZ/ N_2 -purge/ $\text{H}_2\text{O}/\text{N}_2$ -purge, and the GeO_y subcycle, TDMA Ge/N_2 -purge/ $\text{H}_2\text{O}/\text{N}_2$ -purge, respectively (see the SI for details). Varying the Ge/(Ge + Zn) pulse ratio of the ALD process varied the XRF/RBS $[Ge]/([Ge] +$

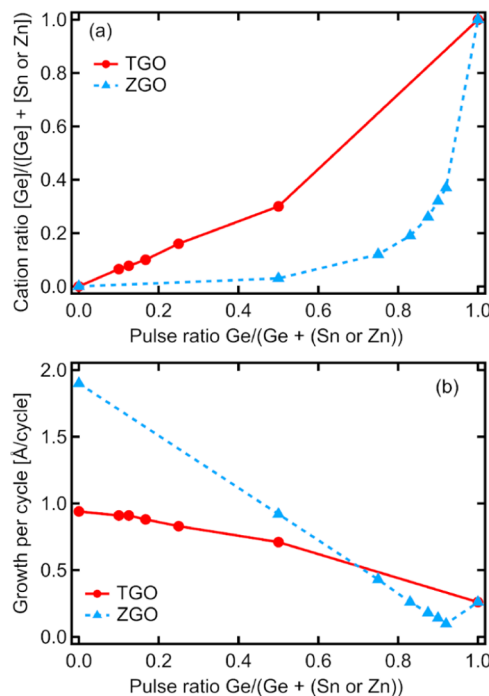


Figure 2. (a) Cation ratio measured by XRF/RBS for TGO and ZGO films in Table 1 as a function of the pulse ratio of the supercycle process. (b) GPC measured by XRR for the TGO and ZGO films (Table S2).

[Zn]) cation ratio, the x -value, measured for films on fused silica, but the film cation ratio severely lags behind the ALD pulse ratio (Figure 2a and Table 1). Figure 2b and Table S2 show that the GPC for these films decreased for an increasing Ge pulse ratio of the ALD ZGO process, even to such an extent that it became substantially lower than for the binary GeO_y and ZnO processes. The QCM data in the SI also showed that the MPC for each GeO_y or ZnO subcycle decreased in the ternary ZGO process. All of these trends suggest that the GeO_y and ZnO subcycles were not fully compatible with each other due to unfavorable surface conditions, which results in a harder-to-control ALD process.

Table 1. Relation between the Study Identification (ID), the Name of the Compound, the ALD Supercycle Pulse Ratio, and the XRF/RBS Cation Ratio

study ID	compound	XRF/RBS cation ratio, x , $[Ge]/([Ge] + [Sn \text{ or } Zn])$	ALD pulse ratio, $Ge/(Ge + (Sn \text{ or } Zn))$
SnO_y	SnO_y	0	0
TGO 0.065	$Sn_{0.935}Ge_{0.065}O_y$	0.065	0.10
TGO 0.077	$Sn_{0.923}Ge_{0.077}O_y$	0.077	0.13
TGO 0.10	$Sn_{0.90}Ge_{0.10}O_y$	0.10	0.17
TGO 0.16	$Sn_{0.84}Ge_{0.16}O_y$	0.16	0.25
TGO 0.30	$Sn_{0.70}Ge_{0.30}O_y$	0.30	0.50
GeO_y	GeO_y	1	1
ZnO	ZnO	0	0
ZGO 0.032	$Zn_{0.968}Ge_{0.032}O_y$	0.032	0.50
ZGO 0.12	$Zn_{0.88}Ge_{0.12}O_y$	0.12	0.75
ZGO 0.19	$Zn_{0.81}Ge_{0.19}O_y$	0.19	0.83
ZGO 0.26	$Zn_{0.74}Ge_{0.26}O_y$	0.26	0.88
ZGO 0.32	$Zn_{0.68}Ge_{0.32}O_y$	0.32	0.90
ZGO 0.37	$Zn_{0.63}Ge_{0.37}O_y$	0.37	0.92
GeO_y	GeO_y	1	1

An interruption experiment was performed to further understand the dynamics of the inhibition seen when mixing ZnO and GeO_y subcycles into ZGO supercycles. A ZnO process was interrupted after 200 cycles with one cycle of GeO_y before continuing with another 200 cycles of ZnO . Similarly, an alternate experiment with 200 cycles of GeO_y , interrupted by one cycle of ZnO before continuing with 200 cycles of GeO_y was also performed. Figure 3 shows the

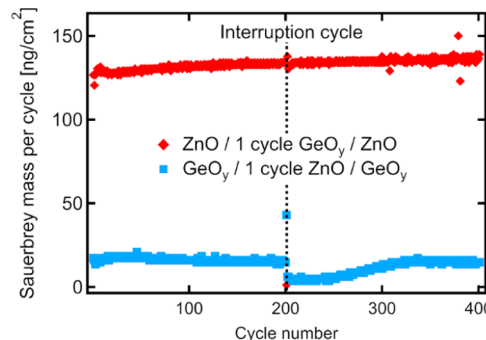


Figure 3. MPC for 400 ALD cycles of either ZnO (red diamonds) or GeO_y (blue squares). The deposition of ZnO was interrupted after 200 cycles by performing a single GeO_y cycle before depositing another 200 cycles of ZnO . Similarly, the deposition of GeO_y was interrupted after 200 cycles by performing a single ZnO cycle before depositing another 200 cycles of GeO_y .

resulting MPC of the two interruption experiments. Only a minor transient in MPC was seen after the ZnO process was interrupted with a single GeO_y cycle. In contrast, when the GeO_y process was interrupted by a single ZnO cycle, the MPC was lowered for more than 100 consecutive GeO_y cycles. Based on this interruption experiment and the general trends in GPC and MPC for the ZGO process, we speculate that exposing the GeO_y surface to DEZ poisons a significant amount of $s^*-Ge-OH$ reaction sites by binding C_2H_5 directly to Ge. We further speculate that the direct bond between Ge and C_2H_5 is strong enough to prevent its reaction with H_2O in subsequent cycles at this deposition temperature of 120 °C, which is relatively low compared to previously published ALD GeO_y processes.^{35–38} The implication of this for the ZGO supercycle processes would be that the more the GeO_y cycles used in a

row, the more the Ge–OH on the surface and the more the reaction sites end up being poisoned during the DEZ exposure. As a result, the GPC would decrease as the amount of GeO_y cycles in the ZGO supercycle increases.

Film Properties. The GeO_y film had a resistivity value of more than $0.26 \Omega \text{ m}$, the upper limit of the 4PP for a 26 nm film, and appears amorphous in grazing incidence X-ray diffraction (GI-XRD) diffractograms (Figure 4). These proper-

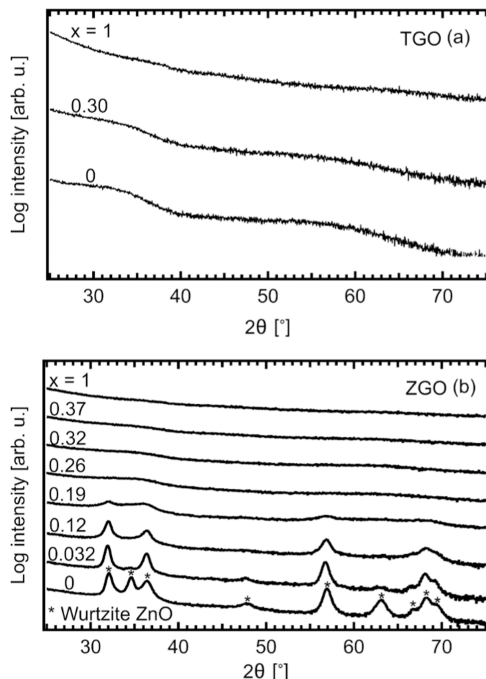


Figure 4. GI-XRD diffractograms of (a) TGO, and (b) ZGO films deposited on fused silica as a function of the cation ratio, x .

ties are similar to GaO_y and SnO_y grown by ALD at the same temperature using metal–organic precursors with the same dimethylamine (DMA) ligand.^{11,39} No optical absorption was detected for GeO_y below 6.2 eV, which was the setup limit. The valence band (E_v) spectrum recorded for GeO_y , as shown in Figure 5, indicates a shift of the E_v for GeO_y toward higher binding energies compared to those for ZnO and SnO_y , representing a shift away from the Fermi level (E_F).

All of the 35–38 nm thick ternary TGO films had resistivity values of more than $0.38 \Omega \text{ m}$, which is the upper limit of the 4PP for 38 nm thick films. The GI-XRD diffractograms (Figure 4a) showed an amorphous morphology for the SnO_y and TGO 0.30 films. It is not surprising to see that TGO 0.3 was both resistive and X-ray amorphous, given that its growth consists of subcycles of SnO_y and GeO_y that also share these properties. Similarly, the SEM cross-sectional micrographs of $\text{ZnO:Al}/\text{ZnO/TGO/ACIGS}$ stacks (Figure 7) showed no indication of crystallinity for SnO_y and TGO 0.10. As the films were amorphous, an indirect E_g model⁴⁰ was used to determine the optical band gap of the TGO films (Figure 6a). Figure 6a and Table S2 show that the E_g slowly increased as the cation ratio increased. In contrast, the measured XPS E_v spectra (Figure 5a) were similar to large tails for all of the measured TGO films, even for the SnO_y . This would suggest that the E_v position at the sample surface is very similar for the investigated TGO samples. It cannot, however, be excluded that the E_v position may vary in the bulk of the samples. To

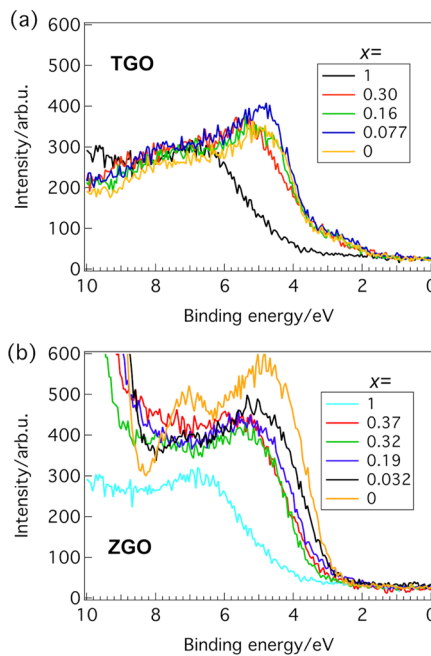


Figure 5. XPS E_v spectra of the investigated (a) TGO and (b) ZGO films deposited on fused silica with varying cation ratios, x .

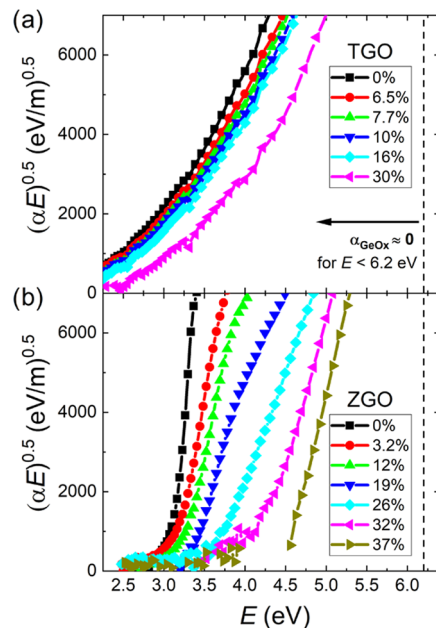


Figure 6. Optical absorption as a function of the cation ratio, x , of (a) TGO and (b) ZGO films deposited on fused silica.

facilitate the relative comparison between samples and exclude charging effects, the binding energy scale was aligned to the C 1s peak of adventitious carbon at 285.0 eV. This also resulted in an energy scale alignment of the shallow core levels for the TGO sample series. Assuming that the E_v of the surface is representable for the bulk and that the electronic and optical E_v 's are identical, the increasing E_g and the identical E_v position suggest that E_c shifts upward as the Ge content of the films increases. A schematic summary of the band trends is shown in Figure 8a, where the positions with regard to ACIGS are roughly estimated from the optically measured E_g and XPS E_v shifts measured in this study and the previously published band

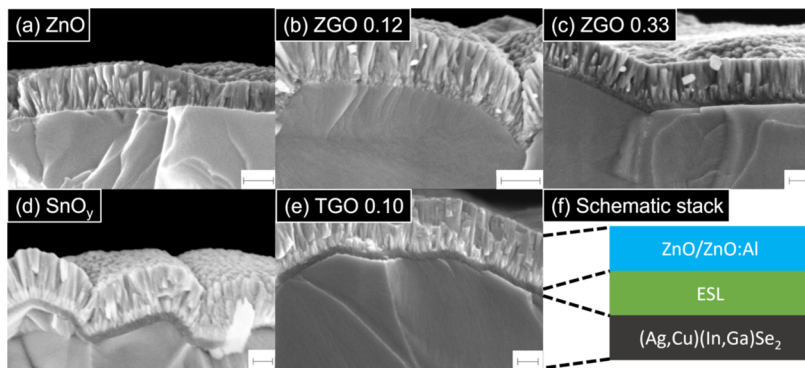


Figure 7. SEM micrographs of the ZnO:Al/ZnO/ESL/ACIGS stacks, where the ESL is (a) ZnO, (b) ZGO 0.12, (c) ZGO 0.33, (d) SnO_y , and (e) TGO 0.10. The scale bar represents 200 nm in (a) and (b) and 100 nm in (c)–(e). (f) Schematic illustration of the ZnO:Al/ZnO/ESL/ACIGS stack.

position for the SnO_y/CIGS interface and ACIGS (eqs S1 and S2).^{22,41} The TGO sample set also showed a noteworthy correlation between the large tailing observed in the optical absorption and XPS E_v spectra, the high resistivity, and the amorphous nature of these films. Compared to the previous study using a high-temperature ALD process,⁸ the films in this study are similar in terms of being amorphous, showing tails in the optical absorption and an increasing E_c position with increasing Ge content, but are substantially more resistive. In the previous study, the resistivity was found to increase with increasing the Ge content as it reduced the O vacancies. We note that our films are made at lower temperatures with a different precursor selection, which perhaps results in more impurities within the film that could potentially occupy the O vacancy sites and thereby increase the resistivity of the film.

The ZnO film was fairly intrinsic with a resistivity of $19 \text{ m}\Omega \text{ m}$, but adding a small amount of Ge as for the ZGO 0.032 film decreased the resistivity to $0.13 \text{ m}\Omega \text{ m}$. Increasing the Ge content further increased the resistivity until it exceeded the 4PP measurement range for the ZGO 0.26 film, where it was larger than $0.45 \text{ }\Omega \text{ m}$ (Table S2). From GI-XRD, the low-Ge content ZGO films had wurtzite ZnO peaks that gradually weakened as the amount of Ge was increased (Figure 4b). Increasing the Ge content further gave X-ray amorphous films. The SEM micrographs (Figure 7) of ZnO:Al/ZnO/ZGO/ACIGS stacks showed a similar trend in terms of the observed crystallinity of the ZGO film. For ZnO, it was hard to make out where the ESL ends and the sputtered ZnO:Al/ZnO stack begins. ZGO 0.12 showed distinct but smaller crystal grains compared to the ZnO:Al/ZnO stack, whereas ZGO 0.30 showed no obvious crystal grains. While the low-cation-ratio ZGO films likely have direct E_g , there was a transition toward X-ray amorphous films for higher cation ratios, which are likely to give them indirect E_g . For simplicity, all of the E_g values of ZGO were therefore estimated using an indirect E_g model. Using the indirect model, Figure 6b and Table S2 clearly show that E_g increased as the ZGO cation ratio increased. The crystallinity, resistivity, and E_g trends were all consistent with two recent publications on ZGO synthesis by ALD using different precursors³⁵ and by chemical vapor deposition (CVD),²⁵ where the ZnO was found to be able to incorporate small amounts of Ge into the wurtzite lattice and thereby increase both conductivity and E_g while larger amounts led to a high resistivity and worse crystal quality. One noticeable difference compared to these earlier studies is that these material property trends occur at higher Ge contents in our

study. However, both the aforementioned ALD study³⁵ and a sputter study on ZGO⁴² showed that the growth conditions such as deposition temperature had high influence on the morphology and electron affinity of the resulting ZGO films. The measured XPS E_v spectra indicated small differences between the ZGO sample series with the addition of Ge (Figure 5b). Similar to the TGO sample series, the binding energy scale has been aligned to the C 1s peak at 285 eV to facilitate comparison between the samples and to exclude any charging effects. Increasing the Ge content, the E_v at the surface of the samples seems to shift slightly toward higher binding energies. While this shift was not observed for the previously CVD grown ZGO with increasing Ge content,²⁵ we noticed that the E_v position for GeO_y is clearly shifted away from ZnO in this study and we did thus not find it unreasonable that E_v for the intermediate ZGO films would be positioned in between. Assuming that E_v does not vary too much in the bulk versus the near-surface region of the films and that the electronic and optical E_g 's are identical, we can compare the E_v results to the optical measurements, as shown in Figure 6b. The E_g increase observed with increasing Ge content is comparable to the measured shift in E_v . However, it becomes larger for higher Ge contents, suggesting that the E_c shifts upward. Figure 8b shows a schematic summary of the suggested band shifts. Their positions as a function of the Ge content and with regard to ACIGS are roughly estimated based on the measured optical E_g and the measured XPS E_v shifts of this study and the previously measured band positions of the ZnO/CIGS interface and ACIGS (eqs S3 and S4).^{22,41} Similarly, for TGO, the ZGO sample set also shows interesting correlations between different sample properties. At low Ge contents, the ZGO films are polycrystalline, have well-defined optical absorption and XPS E_v spectra, and have measurable resistivity. As the Ge content increases and the films become less crystalline, they show increased tailing in optical absorption and XPS E_v spectra and increased resistivity.

Solar Cells. To evaluate the potential of TGO as an ESL, it was deposited with various Ge contents directly onto RbF-treated ACIGS absorbers in ZnO:Al/ZnO/TGO/ACIGS/Mo/SLG solar cell stacks. Until TGO 0.10, the V_{oc} of the solar cells increased with increasing Ge content (Table 2 and Figure SSa). At the same time, the short circuit current density (J_{sc}) (Table 2 and Figures SS c and S7a) remained unchanged, while the fill factor (FF) showed a peak at TGO 0.077 (Table 2 and Figure SSb). For TGO 0.16, both the V_{oc} and the FF started to drop off due to a kink in the $J-V$ curve around V_{oc}

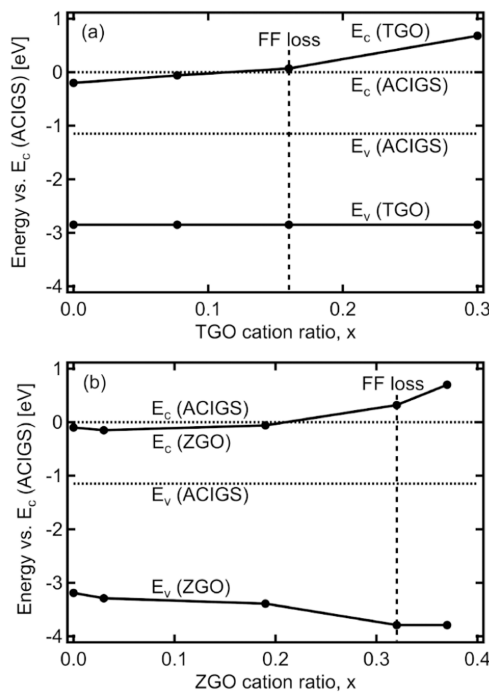


Figure 8. Schematic illustration of the roughly estimated E_c and E_v trends as a function of the cation ratio, x , of (a) TGO and (b) ZGO. The estimations are based on the optical absorption and the XPS E_v spectra from this study and from the SnO_y/CIGS , and ZnO/CIGS band offset and ACIGS band position data from previous studies.^{22,41} The cation ratio where the ACIGS solar cells (see the next section) start showing FF losses is also indicated.

Table 2. Statistical Performance (Average \pm Standard Deviation) of Solar Cells Using TGO ESLs

ESL	V_{oc} (mV)	J_{sc} (mA/cm^2)	FF (%)	efficiency (%)
SnO_y	520 ± 8	30.1 ± 2	63.3 ± 0.5	9.89 ± 0.5
TGO 0.065	581 ± 9	30.0 ± 2	64.0 ± 1	11.2 ± 0.6
TGO 0.077	606 ± 20	30.6 ± 2	65.5 ± 1	12.1 ± 0.7
TGO 0.10	636 ± 7	30.5 ± 2	64.8 ± 1	12.5 ± 0.7
TGO 0.16	621 ± 10	30.7 ± 2	53.8 ± 3	10.3 ± 0.8
TGO 0.30	403 ± 40	1.22 ± 0.4	11.8 ± 0.7	0.06 ± 0.02
CdS	738 ± 3	30.4 ± 2	75.0 ± 0.6	16.8 ± 1

as illustrated by a representative cell in Figure 9a. Finally, the solar cells with TGO 0.30 show low FF, low V_{oc} and a tiny J_{sc} (Figures 9a and S7a), suggesting that the transport of photoexcited electrons has been almost completely hampered. Since J_{sc} remains fairly unchanged up to TGO 0.16 (Table 2 and Figure S5c), the conversion efficiency (Table 2 and Figure S5d) followed the $V_{oc} \times \text{FF}$ product and peaked at TGO 0.10. By comparison, reference solar cells using a CdS ESL showed similar J_{sc} but higher V_{oc} and FF. While the J_{sc} was similar for the TGO films, the EQE showed blue light absorption losses for CdS due to its low E_g of 2.4 eV. There was also a difference between CdS and TGO films for the position of the interference oscillations due to different $\text{ZnO}/\text{Al}/\text{ZnO}/\text{ESL}$ stack thicknesses. Comparing the dark JV to the light JV (Figure S6a) for this sample set, the cation ratios up to TGO 0.10 showed no crossover. The TGO 0.16 sample showed both crossover and a kink that was only apparent in light JV. Curiously, TGO 0.30 appeared to have a light sensitive breakdown voltage. In the logarithmic scale (Figure S6b), all of the TGO ESLs up to 0.16 had similar steepest slopes but not

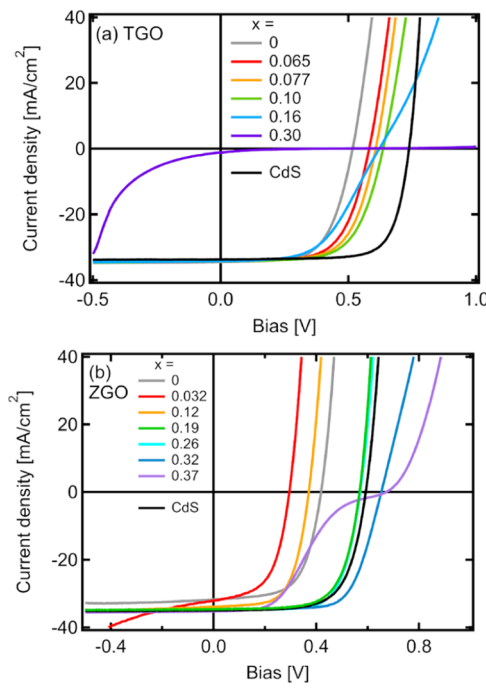


Figure 9. JV sweeps of representative solar cells using (a) TGO and (b) ZGO ESLs.

as steep as the CdS reference. When trying to fit these curves to a single diode model, only the devices without kinks, thus the ones with low Ge contents, gave reasonable fits. For these devices, the ideality factor (n), the saturation current density (J_0), and the series resistance (R_s) were found to be larger and the parallel resistance (R_p) was found to be smaller compared to the CdS reference (Table S3). While the solar cell with CdS was still not ideal, the lower n , J_0 , and R_s and higher R_p can at least partially explain the superior V_{oc} and FF compared to the ones with TGO ESLs.

The ZGO films were evaluated as potential ESL candidates by depositing them directly on ACIGS and measuring the performance of the $\text{ZnO}/\text{Al}/\text{ZnO}/\text{ZGO}/\text{ACIGS}/\text{Mo}/\text{SLG}$ solar cell stacks as a function of the Ge content. As the Ge content was increased for the ZGO films, the solar cells showed a decrease in V_{oc} compared to solar cells using ZnO (Table 3 and Figure S8a). When the Ge content increased further, there was an increase in V_{oc} up to ZGO 0.37. The FF followed a similar trend (Table 3 and Figure S8b) but started dropping off for the ZGO 0.33 ESL and showed an even lower value for ZGO 0.37 due to a severe double diode that vastly reduces the FF (Figure 9b). A small gain in J_{sc} was observed as the Ge content increased from ZnO up to ZGO 0.12, whereas

Table 3. Statistical Performance (Average \pm Standard Deviation) of Solar Cells Using ZGO ESLs

ESL	V_{oc} (mV)	J_{sc} (mA/cm^2)	FF (%)	efficiency (%)
ZnO	412 ± 8	28.3 ± 1	60.1 ± 5	7.03 ± 0.7
ZGO 0.032	296 ± 20	29.0 ± 1	53.5 ± 4	4.60 ± 0.5
ZGO 0.12	375 ± 9	30.3 ± 0.8	62.0 ± 2	7.06 ± 0.4
ZGO 0.19	563 ± 40	30.4 ± 1	68.2 ± 3	11.7 ± 1
ZGO 0.26	568 ± 20	30.3 ± 1	70.7 ± 2	12.2 ± 0.8
ZGO 0.32	644 ± 30	30.6 ± 1	68.2 ± 4	13.4 ± 1
ZGO 0.37	628 ± 100	30.6 ± 2	31.8 ± 10	6.29 ± 3
CdS	590 ± 6	31.4 ± 1	67.2 ± 2.4	12.5 ± 0.7

it stayed relatively constant afterward (Table 3 and Figures S7b and S8c). From EQE (Figure S3b), the lower J_{sc} was due to a lower response from 330 up to approximately 800 nm. Since it was lower for shorter wavelengths, electron–hole pairs generated close to the ESL/ACIGS interface must, to a larger extent, recombine prior to being collected at the contacts. This suggests that the ESL/ACIGS interface recombination was large. The EQE also showed that the interference peaks shifted to slightly different wavelengths, which was likely due to the varying ESL thickness (Table S2). Similarly, the CdS reference showed a different interference pattern and blue light loss due to its 2.4 eV E_g . While the resulting conversion efficiency (Table 3 and Figure S8d) was somewhat affected by J_{sc} at lower Ge contents, it was mostly defined by the $V_{oc} \times FF$ product. The $V_{oc} \times FF$ product and the efficiency peaked for the ZGO 0.32 ESL, where the FF had only decreased a bit and where the V_{oc} was still increasing with the Ge content. While the ZGO 0.33 ESL in this case outperformed the reference CdS ESL with regard to solar cell efficiency, it is important to remember that the ACIGS surface of this series was not post-treated with RbF prior to the deposition of CdS or ZGO. It is worth noting that the spread in solar cell performance was larger when using a ZGO ESL instead of a TGO ESL (Tables 2 and 3; Figures S5 and S8). In the extreme case of the ZGO 0.37 ESL, the spread originated from fairly continuous trends in FF, J_{sc} , and V_{oc} across the sample, suggesting that the film did not have the same ZGO cation ratio for all cells. Perhaps this nonuniformity was related to the previously discussed inhibition issues of the ALD ZGO processes. The dark JV of this sample set (Figure S9a) did in general not show crossover with the light curves. An exception to this was ZGO 0.37, which showed a minor crossover at forward bias and a different light JV curvature at reverse bias compared to the dark JV. From the logscale of the dark JV (Figure S9b), it was apparent that the lower ZGO cation ratios gave larger saturation or even shunt currents. It is not unreasonable to think that these currents are facilitated through recombination sites at the ESL/ACIGS interface that were shown to be active in EQE. In general, the steepest slopes of the dark JV curves of the solar cells in this sample set were quite small and very similar between the different cation ratios, suggesting that they were fundamentally limited by similar recombination if the high saturation and shunt currents were excluded. While it was only possible to model the devices with intermediate Ge contents using a single diode model, they showed similar n , J_0 , R_s , and R_p to the CdS references, confirming the dark JV observations. Perhaps this suggests that the lack of RbF treatment of this particular ACIGS absorber rather than the ESL choice imposed the upper limit for the solar cell performance of this sample set.

The volcano trends in V_{oc} and FF as the Ge content increases for TGO and ZGO ESLs resemble the results from the previous study on ZGO²⁵ and the studies on Zn(O,S), (Zn,Mg)O, ZTO, ZnIn_xS_y, ZnTiO, TGAO, and In₂(S,O)₃ ESLs with varying E_c positions on ACIGS absorbers.^{10–15} The main theory for these trends has been that the ACIGS solar cells are very sensitive to the placement of the ESL E_c . Placing it beneath the ACIGS E_c was proposed to increase the ESL/ACIGS interface recombination. This is due to the band bending of the ESL and the ACIGS that in general places the p–n junction directly at the ESL/ACIGS interface, thereby increasing the interface recombination probability. By shifting the E_c further up the band bending forces the p–n junction

away from the ESL/ACIGS interface and into the ACIGS, thereby lowering the probability of interface recombination. In addition, as the ESL E_c shifts further up in energy, the resulting ESL band bending further prevents the diffusion of electrons directly from the transparent conductive oxide (TCO) to the ESL/ACIGS interface. The effectiveness of this depends on the ESL doping though, where higher doping not only increases the majority carriers within the ESL but also reduces the barrier for diffusion from the TCO. Perhaps this is why the low-resistivity ZGO films showed a lower V_{oc} and indications of a higher interface recombination in the EQE, light JV, and dark JV (Figures S6, S7, and S9) compared to the high-resistivity TGO films with similarly low E_c positions. In general, the effects of shifting E_c up mitigate the interface recombination and lead to an increased V_{oc} , which has previously been verified both experimentally and through modeling.^{10,14,43–49} In this study, the XPS E_v spectra and the optically determined E_v suggested that the effective E_c shifts upward with increasing Ge content of ZGO and TGO (Figure 8). With this in mind, the solar cell results showed that V_{oc} does, in general, increase as E_c shifts higher in the ZGO and TGO ESLs. Previous studies also showed that placing the ESL E_c above the ACIGS E_c created an energy barrier for the photoexcited electrons to traverse as they are extracted from the ACIGS. If the barrier becomes too high, larger than 0.3 eV, it was observed to induce a bias-dependent electron transfer across the interface, seen as a kink in the JV curve, and a reduced FF.^{10,14,43–50} This injection barrier seen from the ACIGS to ESL is, however, dependent on band bending and effectively decreases when the doping of the ESL is high. A similar decrease in FF due to a kink in JV appeared in this study when using the TGO 0.16 or ZGO 0.37 ESL, suggesting that the effective E_c was shifted too high in these ESLs. Relating these ESL back to their roughly estimated band positions, shown as the point with FF loss in Figure 8, they do indeed create barriers toward the ACIGS. While this occurred for slightly different barrier heights according to Figure 8, it is important to remember that the band placements are estimates and that we do not know the effective barrier height as the doping of TGO 0.16 and ZGO 0.37 is not known. Shifting E_c even higher has been shown to enhance the kink, and in the extreme case, the energy barrier became so large that almost no electrons were able to cross the interface and leave the ACIGS, which vastly reduced the J_{sc} and V_{oc} .^{9,44,47,49} This behavior was reproduced when TGO 0.30 was used, which was the ESL with the highest effective E_c of the TGO films (Figure 8). This sample also showed a vastly reduced dark current (Figure S6), suggesting that the barrier was so high that it hampers not only the injection from the ACIGS to the TCO but also the diffusion of electrons from the TCO to the ACIGS even at substantial forward bias. Due to the tradeoff between an increased V_{oc} and a lowered FF, previous studies have observed that the best performance was achieved when the ESL E_c was placed at the same level or slightly above the ACIGS E_c .^{10,43–50} In this study, the best devices were found for the ZGO 0.32 and TGO 0.10 ESLs, both just after the onset of the FF losses. Thus, our observed trends in FF and V_{oc} indicate that we successfully shifted and found good E_c positions for TGO and ZGO by varying their cation ratios.

A direct comparison between the TGO and ZGO ESLs was performed on the same RbF-treated ACIGS absorber using some of the best ZGO and TGO cation ratios. In addition, both Zn_{0.8}Sn_{0.2}O_y (ZTO 0.2)¹¹ and CdS were also used as ESL

references on the same ACIGS. Prior to the *JV* sweeps, the solar cells were exposed to 24 h of light soaking under 1 sun without active cooling to enhance their performance.^{26,51} Despite having good E_c alignments, the solar cells with ZGO 0.32 and TGO 0.077 ESLs had lower FF and V_{oc} compared to CdS (Table 4 and Figures 10a, S10, and S11). The solar cells

Table 4. Statistical Performance (Average \pm Standard Deviation) of Solar Cells Using Different ESLs

ESL	V_{oc} (mV)	J_{sc} (mA/cm ²)	FF (%)	efficiency (%)
TGO 0.077	654 \pm 5	30.7 \pm 1	64.2 \pm 0.8	12.9 \pm 0.5
TGO 0.077 TMA	695 \pm 4	30.9 \pm 1	63.9 \pm 1	13.7 \pm 0.6
TGO 0.077 ZnS	702 \pm 4	31.9 \pm 1	61.6 \pm 1	13.8 \pm 0.6
ZGO 0.32	704 \pm 8	31.2 \pm 1	61.3 \pm 7	13.5 \pm 2
ZTO 0.20	711 \pm 9	31.1 \pm 1	72.7 \pm 3	16.1 \pm 1
CdS	747 \pm 3	31.1 \pm 1	74.1 \pm 0.9	17.2 \pm 1

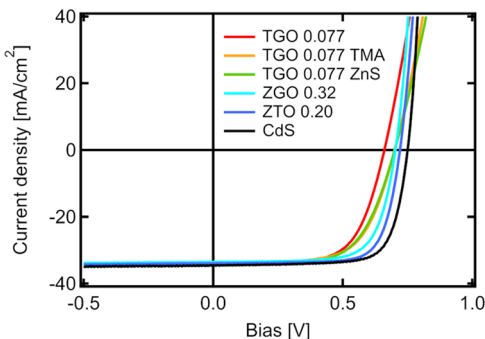


Figure 10. *JV* sweeps for the best solar cells using the same RbF PDT ACIGS absorber and either TGO 0.077, ZGO 0.32, ZTO 0.2, or CdS as the ESL. Scans of solar cells using a pretreatment of either one cycle of ALD Al₂O₃ (TMA + H₂O) or three cycles of ALD ZnS (DEZ + H₂S) prior to the deposition of TGO 0.077 are also shown.

with ZGO 0.32 ESLs had almost the same V_{oc} as those with ZTO 0.2 but, on average, worse FF. There was however a large spread in FF across the sample for ZGO 0.32, perhaps relating back to the uniformity issues of the ALD process. The TGO 0.077 ESL clearly gave lower V_{oc} and FF compared to the Zn- or Cd-containing alternatives, just like in a previous study on TGAO ESL.¹⁴ Aside from the blue losses in EQE for the devices with 2.4 eV E_g CdS, all of the solar cells showed good collection with some variation in the interference peak positions due to the difference in their ZnO:Al/ZnO/ESL stack thicknesses. This resulted in similar J_{sc} values for the different solar cells. There was no crossover between the dark and light *JV* for this sample set (Figure S12). The single-diode fit to the dark *JV* showed a correlation between having a low n and J_0 and measuring a high V_{oc} (Table S5). This confirms that V_{oc} and, to some extent, the FF are limited by ESL-related recombination, e.g., interface recombination. In general, there was not a strong correlation between the modeled R_p and R_s measured FF, suggesting that n was the limiting factor. However, the cells with TGO 0.077 and the worst FF of the set did clearly show both the highest n and R_s values. For the best cells using EQE-corrected current density, the performance was 14.8% for TGO 0.077, 17.0% for ZGO 0.32, 18.2% for ZTO 0.2, and 19.5% for CdS (Table 5). These results were in general in line with the average data, except for ZGO 0.32, which comes closer to ZTO 0.2 and CdS due to only selecting the best cell. As previously shown, it is not trivial to use ALD-

Table 5. Best Solar Cell Performance Using Different ESLs

ESL	V_{oc} (mV)	J_{sc} (mA/cm ²)	FF (%)	efficiency (%)
TGO 0.077	661	34.0 (EQE)	65.8	14.8
TGO 0.077 TMA	700	33.9 (EQE)	65.2	15.5
TGO 0.077 ZnS	700	34.5 (EQE)	63.5	15.3
ZGO 0.32	703	33.7 (EQE)	71.8	17.0
ZTO 0.20	721	33.6 (EQE)	75.0	18.2
CdS	751	34.6 (EQE)	75.2	19.5

based ESLs on alkali halide-treated ACIGS surfaces, and they do, in general, come short of chemical bath-based alternatives, e.g., CdS, because of this.³² However, previous studies also showed that the ability of the ALD ZTO ESL to shift its E_c up enables a higher V_{oc} compared to CdS for absorbers where the E_c resides higher, e.g., ACIGS with high Ga content, Cu(In,Ga)S₂, and CZTS.^{18–21} Even with the ZTO ESL, these solar cells still showed large V_{oc} deficits, which was partially believed to be due to the ZTO not fully being able to push its E_c all the way up to match the absorber E_c . Therefore, it is very encouraging to see that ZGO, with its ability to shift E_c even further up, comes so close in performance to ZTO in this initial study.

Even with a favorable E_c position, the TGO 0.077 ESL still gave lower V_{oc} and FF compared to the other ESL options. One thing that clearly distinguishes the TGO process from the more successful ALD ESL is that it does not contain Zn or its very reactive precursor DEZ. In the first test, the initial ALD conditions of Zn-containing ESLs were therefore mimicked by using three ALD cycles of ZnS (DEZ and H₂S) before continuing on with a TGO 0.077 ESL. The resulting *JV* data for these solar cells (Tables 4 and 5; Figures 10, S10, and S11) show that V_{oc} improved to values comparable to using ZGO 0.32 ESL. Such an effect is in line with previous studies where thin ZnS interlayers at the ESL/CIGS interface improved V_{oc} by lowering the recombination.^{9,52} While not completely understood, some studies have suggested that Zn reacts with the surface and occupies Cu vacancies that are prevalent on these absorbers. This effectively dopes the surface n-type and has been suggested to push the p–n junction into the absorber and thus lower the influence of interface recombination.^{53–55} To test if this V_{oc} gain was exclusive to using a DEZ + H₂S exposure of the ACIGS surface, a similar exposure test was performed with a single Al₂O₃ ALD cycle (Al(CH₃)₃ (trimethylaluminum, TMA) and H₂O). The resulting V_{oc} for these cells also became comparable to that for ZGO 0.32 (Tables 4 and 5; Figures 10, S10, and S11). While there are no studies suggesting a diffusion of Al into ACIGS, there are studies where such an exposure led to native surface oxides being converted into Al₂O₃ that ends up passivating the interfaces by either removing recombination paths or by the inherent fixed charge of the Al₂O₃ repelling charge carriers away.^{56–59} The V_{oc} gain was thus not exclusive to using DEZ in the ALD process, but perhaps such pretreatments that electrically passivate the ACIGS surface before the TGO process starts growing or change the chemistry of the TGO film at the interface are required to form a good interface. The two pretreatments did, however, not improve the FF of the ACIGS solar cells (Figures S12a and S4b). This agrees with the single-diode fitting of the dark *JV*, where neither the n nor the R_s changes with the pretreatments (Table S5). Compared to the other solar cells of the series, the R_s was distinctly higher for all of the solar cells with TGO ESLs (Table S5). As

mentioned in the [Film Properties](#) section, it was not possible to measure the bulk resistivity for the TGO 0.077, and ZGO 0.32 films to investigate whether an extra series resistance could stem from the bulk of the ESL. However, when comparing solar cells with TGO 0.10 ESLs using 402 and 204 cycles ([Figure S13](#)), there is no difference in FF, suggesting that the bulk resistivity has a negligible effect. This is similar to what was previously observed for amorphous TGAO ESLs.¹⁴ An increased series resistance could also stem from having increased contact resistance at either the ESL/ACIGS or the ZnO/ESL interface. The contact resistance decreases with doping of the materials. While the bulk resistivities are high for both TGO and ZGO, it is possible that their doping levels vary and that, e.g., it is low enough for TGO to increase the contact resistance to ACIGS and ZnO. It would therefore be interesting to further investigate whether other treatments of the ACIGS could also improve FF and whether treating the ESL prior to the ZnO deposition has an effect on FF.

From the results on ZGO and TGO ESLs, we are able to gain several insights into the previous success of ZGO and Zn-containing ALD ESLs in general. We note that the best solar cells using ZGO 0.32 ESLs give slightly lower V_{oc} and FF compared to ZTO ESLs, whereas solar cells with TGO ESLs fall short in these parameters. From this, we can deduce that an ALD process including Zn seems to be beneficial for the ACIGS and that the choice of the other cation, Sn or Ge in this case, seems less influential. The surface exposures of the ACIGS surface using DEZ + H₂S or TMA improves V_{oc} for devices with TGO. This suggests that when DEZ or a precursor of similar reactivity, e.g., TMA, is used in the ALD process, the ESL/ACIGS interface quality is improved by the precursor exposure of the ACIGS surface during ESL film nucleation. Solar cells using ZGO ESLs are also able to achieve similar FF to those with ZTO 0.2, whereas the ones with TGO once more fall short, even after the aforementioned surface treatments. Based on the dark JV, this seems to stem from an increased series resistance, and it aligns well with previous studies where TGAO falls short in FF due to a high series resistance¹⁴ and where (Zn,Mg)O and Zn(O,S) achieve similar performance to their CdS references.^{9,10,60,61} The fully amorphous nature of TGO and TGAO suggests that their bulk resistivity could be high, but it has been shown, both in this study for TGO and in a previous study on TGAO, that this is not what limits the FF. Instead, the previous study on TGAO suggested that the series resistance must stem from the interfaces to ACIGS and ZnO, which this study also finds to be a plausible cause for the low FF. In comparison, it seems that the Zn-containing processes are able to create low contact resistances to both the ACIGS and the ZnO window stack.

From these observations, we note three main criteria that need to be met for making good ESLs for ACIGS that the Zn-containing ESLs in general have: First, a good E_c alignment between the ESL and the absorber to minimize the influence of interface recombination and to avoid blocking excited electrons exiting the absorber; second, high interface quality between the ESL and ACIGS, which electrically passivates recombination paths there; and finally, the bulk of the ESL likely needs to form interfaces with low contact resistance toward the ACIGS and ZnO to not affect the series resistance of the solar cell. In this study, we have shown that ZGO is able to decently fulfill all three of them, while TGO falls short of the latter two. It is however important to remember that the criteria are very dependent on the absorber material and that

the TGO perhaps can work better if proper pretreatments of the underlying material and post-treatments of the TGO are performed to mitigate its issues with the latter two criteria.

CONCLUSIONS AND OUTLOOK

An ALD process for GeO_y was developed at 120 °C using TDMAGe and H₂O. The GeO_y process was then used to create ALD TGO and ZGO supercycle processes by mixing it with previously established SnO_y and ZnO processes, respectively. By varying the Ge content of the ZGO and TGO films, their electrical, optical, and morphological properties changed. TGO remained highly resistive and amorphous for all Ge contents, whereas ZGO showed increased resistivity and reduced wurtzite crystallinity as the Ge content increased. The combined results from XPS and optical absorption suggested that the effective E_c shifts upward for both TGO and ZGO as the Ge content increased. This finding was tested for ACIGS solar cells, which are sensitive to the E_c alignment between the absorber and the ESL. For both TGO and ZGO, the general trend with increasing E_c was that V_{oc} and thereby the solar cell efficiency increased. At some point, increasing the E_c position further up started to block electron transport from the absorber into the ESL, which decreased FF. The resulting solar cell efficiency as a function of the E_c shifting up resembled a volcano plot where the ESL from the peak region gave efficiency values of up to 17.0% for ZGO 0.32 and 14.8% for TGO 0.077 (19.5% CdS, 18.2% ZTO). The promising performance of ZGO as an ESL in ACIGS solar cells, coupled with the ability to shift E_c higher than previously possible with ZTO, makes it very interesting to try out for related high- E_c absorbers such as Cu₂ZnSnS₄, Cu₂ZnGeS₄, Cu(In,Ga)S₂ and (Ag,Cu)GaSe₂. However, the ALD chemistry used in this study limited the growth rate and uniformity of the films. Thus, to fully use the potential of the high-Ge-content ZGO, a different ALD chemistry would need to be developed at this low deposition temperature or an alternative growth method would need to be used, such as CVD, pulsed laser deposition, or sputtering, which have previously shown promising results for Cu₂O and BaSi₂ absorbers, respectively.^{24,25,42} In contrast, the TGO ALD process worked very well and there was no obvious hurdle to further increase the Ge content of the resulting films. While using these films as ESLs in ACIGS solar cells does not give the best performance, they are interesting ESL candidates for perovskite solar cells for several reasons. They do not contain Zn that reacts with the perovskite at the ESL/perovskite interface,⁶² they can change their E_c position in a wide range and thereby match a variety of perovskite E_c , and they use a very similar ALD chemistry to SnO_y that has already shown great success as an ESL in perovskite solar cells.⁶³

ASSOCIATED CONTENT

Supporting Information

The Supporting Information is available free of charge at <https://pubs.acs.org/doi/10.1021/acsaem.3c00960>.

Detailed ALD development for GeO_y, TGO and ZGO processes with pulse and purge dynamics, Sauerbrey mass readout from the QCM during TGO and ZGO processes, tabulated TGO and ZGO film properties, EQE graphs, dark JV and single-diode fit parameters for the solar cells with TGO or ZGO ESLs, and statistical solar cell performance data for ESL comparison ([PDF](#))

AUTHOR INFORMATION

Corresponding Author

Adam Hultqvist — Division of Solar Cell Technology, Department of Materials Science and Engineering, Uppsala University, 75103 Uppsala, Sweden;  orcid.org/0000-0002-2402-5427; Email: adam.hultqvist@angstrom.uu.se

Authors

Jan Keller — Division of Solar Cell Technology, Department of Materials Science and Engineering, Uppsala University, 75103 Uppsala, Sweden

Natalia M. Martin — Division of Solar Cell Technology, Department of Materials Science and Engineering, Uppsala University, 75103 Uppsala, Sweden;  orcid.org/0000-0002-6881-4989

Fredrik Larsson — Evolar AB, 75651 Uppsala, Sweden

Tobias Törndahl — Division of Solar Cell Technology, Department of Materials Science and Engineering, Uppsala University, 75103 Uppsala, Sweden;  orcid.org/0000-0001-7757-5847

Complete contact information is available at:

<https://pubs.acs.org/10.1021/acsaem.3c00960>

Author Contributions

A.H. wrote the manuscript, developed the ZGO process using QCM, continued the development of the TGO and GeO_y processes using QCM, measured XRF and film resistivity, finished the solar cell stacks, and measured the solar cell performance. J.K. measured and calculated the optical properties and was especially involved in the discussion regarding the optical properties and solar cell performance. N.M.M. performed the XPS measurements, directed the HAXPES measurements, and mainly partook in the discussion regarding these results. F.L. performed the initial development of the GeO_y and the TGO ALD processes using QCM, and was mainly involved in the discussion regarding the ALD process development. T.T. supervised the project, conducted the XRD analysis, performed XRR measurements, and was involved in the discussion of all the results. All authors have seen the whole content of the manuscript and given their approval to submit the final version.

Notes

The authors declare no competing financial interest.

ACKNOWLEDGMENTS

The authors are thankful for the financial support from the Swedish Energy Agency (Grant Nos. 48 479-1 and P2020-90052) and STandUP for ENERGY. Daniel Primetzhofer at the Department of Physics and Astronomy, Uppsala University, is acknowledged for performing and aiding in the evaluation of the Rutherford backscattering measurements.

REFERENCES

- (1) Zhang, J.; Li, Y.; Cao, K.; Chen, R. Advances in Atomic Layer Deposition. *Nanomanuf. Metrol.* **2022**, *5* (3), 191–208.
- (2) Puurunen, R. L. Surface chemistry of atomic layer deposition: A case study for the trimethylaluminum/water process. *J. Appl. Phys.* **2005**, *97* (12), No. 121301.
- (3) Huang, H.; Lv, J.; Bao, Y.; Xuan, R.; Sun, S.; Sneed, S.; Li, S.; Modanese, C.; Savin, H.; Wang, A.; Zhao, J. 20.8% industrial PERC solar cell: ALD Al₂O₃ rear surface passivation, efficiency loss mechanisms analysis and roadmap to 24%. *Sol. Energy Mater. Sol. Cells* **2017**, *161*, 14–30.
- (4) Raiford, J. A.; Oyakhire, S. T.; Bent, S. F. Applications of atomic layer deposition and chemical vapor deposition for perovskite solar cells. *Energy Environ. Sci.* **2020**, *13* (7), 1997–2023.
- (5) Brinkmann, K. O.; Gahlmann, T.; Riedl, T. Atomic Layer Deposition of Functional Layers in Planar Perovskite Solar Cells. *Sol. RRL* **2020**, *4* (1), No. 1900332.
- (6) Sinha, S.; Nandi, D. K.; Pawar, P. S.; Kim, S. H.; Heo, J. A review on atomic layer deposited buffer layers for Cu (In, Ga) Se₂ (CIGS) thin film solar cells: Past, present, and future. *Sol. Energy* **2020**, *209*, 515–537.
- (7) He, M.; Sun, K.; Suryawanshi, M. P.; Li, J.; Hao, X. Interface engineering of pn heterojunction for kesterite photovoltaics: A progress review. *J. Energy Chem.* **2021**, *60*, 1–8.
- (8) Chua, D.; Kim, S. B.; Sinsermsuksakul, P.; Gordon, R. Atomic layer deposition of energy band tunable tin germanium oxide electron transport layer for the SnS-based solar cells with 400 mV open-circuit voltage. *Appl. Phys. Lett.* **2019**, *114* (21), No. 213901.
- (9) Platzer-Björkman, C.; Törndahl, T.; Abou-Ras, D.; Malmström, J.; Kessler, J.; Stolt, L. Zn (O, S) buffer layers by atomic layer deposition in Cu (In, Ga) Se₂ based thin film solar cells: Band alignment and sulfur gradient. *J. Appl. Phys.* **2006**, *100* (4), No. 044506.
- (10) Törndahl, T.; Platzer-Björkman, C.; Kessler, J.; Edoff, M. Atomic layer deposition of Zn_{1-x}Mg_xO buffer layers for Cu (In, Ga) Se₂ solar cells. *Prog. Photovoltaics* **2007**, *15* (3), 225–235.
- (11) Hultqvist, A.; Platzer-Björkman, C.; Zimmermann, U.; Edoff, M.; Törndahl, T. Growth kinetics, properties, performance, and stability of atomic layer deposition Zn–Sn–O buffer layers for Cu (In, Ga) Se₂ solar cells. *Prog. Photovoltaics* **2012**, *20* (7), 883–891.
- (12) Genevée, P.; Darga, A.; Longeaud, C.; Lincot, D.; Donsanti, F. Atomic layer deposition of ZnIn_xS_y buffer layers for Cu (In, Ga) Se₂ solar cells. *J. Renewable Sustainable Energy* **2015**, *7* (1), No. 013116.
- (13) Hwang, S.; Larina, L.; Lee, H.; Kim, S.; Choi, K. S.; Jeon, C.; Ahn, B. T.; Shin, B. Wet pretreatment-induced modification of Cu (In, Ga) Se₂/Cd-free ZnTiO buffer interface. *ACS Appl. Mater. Interfaces* **2018**, *10* (24), 20920–20928.
- (14) Larsson, F.; Keller, J.; Olsson, J.; Donzel-Gargand, O.; Martin, N. M.; Edoff, M.; Törndahl, T. Amorphous tin-gallium oxide buffer layers in (Ag, Cu)(In, Ga) Se₂ solar cells. *Sol. Energy Mater. Sol. Cells* **2020**, *215*, No. 110647.
- (15) Bugot, C.; Bouttemy, M.; Schneider, N.; Etchegorry, A.; Lincot, D.; Donsanti, F. New insights on the chemistry of plasma-enhanced atomic layer deposition of indium oxysulfide thin films and their use as buffer layers in Cu (In, Ga) Se₂ thin film solar cell. *J. Vac. Sci. Technol., A* **2018**, *36* (6), No. 061510.
- (16) Tao, S.; Schmidt, I.; Brocks, G.; Jiang, J.; Tranca, I.; Meerholz, K.; Olthof, S. Absolute energy level positions in tin-and lead-based halide perovskites. *Nat. Commun.* **2019**, *10* (1), No. 2560.
- (17) Wada, T. Materials science of chalcopyrite-type and multinary solar cells compounds: crystal structure and electronic structure of CISe, CZTS, CTS, and the related compounds. *JSAP Rev.* **2022**, *2022*, No. 220204.
- (18) Larsson, F.; Shariati Nilsson, N.; Keller, J.; Frisk, C.; Kosyak, V.; Edoff, M.; Törndahl, T. Record 1.0 V open-circuit voltage in wide band gap chalcopyrite solar cells. *Prog. Photovoltaics* **2017**, *25* (9), 755–763.
- (19) Keller, J.; Stolt, L.; Törndahl, T.; Edoff, M. Silver-alloying in highly-efficient CuGaSe₂ solar cells with different buffer layers. *Sol. RRL* **2023**, *7*, No. 2300208.
- (20) Cui, X.; Sun, K.; Huang, J.; Lee, C. Y.; Yan, C.; Sun, H.; Zhang, Y.; Liu, F.; Hossain, M. A.; Zakaria, Y.; Wong, L. H.; et al. Enhanced heterojunction interface quality to achieve 9.3% efficient Cd-free Cu₂ZnSnS₄ solar cells using atomic layer deposition ZnSnO buffer layer. *Chem. Mater.* **2018**, *30* (21), 7860–7871.
- (21) Sood, M.; Adeleye, D.; Shukla, S.; Törndahl, T.; Hultqvist, A.; Siebentritt, S. Low temperature (Zn, Sn) O deposition for reducing interface open-circuit voltage deficit to achieve highly efficient Se-free Cu (In, Ga) S₂ solar cells. *Faraday Discuss.* **2022**, *239*, 328–338.

- (22) Kapilashrami, M.; Kronawitter, C. X.; Törndahl, T.; Lindahl, J.; Hultqvist, A.; Wang, W. C.; Chang, C. L.; Mao, S. S.; Guo, J. Soft X-ray characterization of $Zn_{1-x}Sn_xO_y$ electronic structure for thin film photovoltaics. *Phys. Chem. Chem. Phys.* **2012**, *14* (29), 10154–10159.
- (23) Afanas'ev, V. V.; Stesmans, A. Energy band alignment at the (100) Ge/HfO₂ interface. *Appl. Phys. Lett.* **2004**, *84* (13), 2319–2321.
- (24) Minami, T.; Nishi, Y.; Miyata, T. Efficiency enhancement using a $Zn_{1-x}Ge_xO$ thin film as an n-type window layer in Cu₂O-based heterojunction solar cells. *Appl. Phys. Express* **2016**, *9* (5), No. 052301.
- (25) Egyna, D.; Ito, S.; Nishimura, T.; Yamada, A. Growth of Zn-Ge-O Thin-Film as a Transparent Conductive Oxide Buffer Material for Chalcopyrite Solar Cell. *Cryst. Res. Technol.* **2023**, *58* (2), No. 2200145.
- (26) Keller, J.; Chalvet, F.; Joel, J.; Aijaz, A.; Kubart, T.; Riekehr, L.; Edoff, M.; Stolt, L.; Törndahl, T. Effect of KF absorber treatment on the functionality of different transparent conductive oxide layers in CIGSe solar cells. *Prog. Photovoltaics* **2018**, *26* (1), 13–23.
- (27) Pool, V. L.; Dou, B.; Van Campen, D. G.; Klein-Stockert, T. R.; Barnes, F. S.; Shaheen, S. E.; Ahmad, M. I.; Van Hest, M. F. A. M.; Toney, M. F. Thermal engineering of FAPbI₃ perovskite material via radiative thermal annealing and in situ XRD. *Nat. Commun.* **2017**, *8*, No. 14075.
- (28) Sauvrey, G. Verwendung von Schwingquarzen zur Wägung dünner Schichten und zur Mikrowägung. *Z. Phys.* **1959**, *155*, 206–222.
- (29) Mecea, V. M. From quartz crystal microbalance to fundamental principles of mass measurements. *Anal. Lett.* **2005**, *38* (5), 753–767.
- (30) Larsson, F.; Stolt, L.; Hultqvist, A.; Edoff, M.; Keller, J.; Törndahl, T. Atomic layer deposition of ternary compounds on Cu (In, Ga) Se₂: an in situ quartz crystal microbalance study. *ACS Appl. Energy Mater.* **2020**, *3* (7), 7208–7215.
- (31) Hong, W. Q. Extraction of extinction coefficient of weak absorbing thin films from special absorption. *J. Phys. D: Appl. Phys.* **1989**, *22* (9), 1384.
- (32) Larsson, F.; Donzel-Gargand, O.; Keller, J.; Edoff, M.; Törndahl, T. Atomic layer deposition of Zn (O, S) buffer layers for Cu (In, Ga) Se₂ solar cells with KF post-deposition treatment. *Sol. Energy Mater. Sol. Cells* **2018**, *183*, 8–15.
- (33) Lindahl, J.; Zimmermann, U.; Szaniawski, P.; Törndahl, T.; Hultqvist, A.; Salomé, P.; Platzer-Björkman, C.; Edoff, M. Inline Cu (In, Ga) Se₂ Co-evaporation for high-efficiency solar cells and modules. *IEEE J. Photovoltaics* **2013**, *3* (3), 1100–1105.
- (34) Sterner, J.; Kessler, J.; Bodegård, M.; Stolt, L. In *Atomic Layer Epitaxy Growth of ZnO Buffer Layers in Cu (In, Ga) Se₂ Solar Cells*, Proceedings of the 2nd World Conference on Photovoltaic Energy Conversion 1998, Vienna, Austria, July 6–10, 1998; Schmid, J.; Ossenbrink, H. A.; Helm, P.; Ehmann, H.; Dunlop, E. D., Eds.; European Commission Directorate General Joint Research Centre Institute Renewable Energies Unit: Italy, 1998; pp 1145–1148.
- (35) Chalker, P. R.; Marshall, P. A.; King, P. J.; Dawson, K.; Romani, S.; Williams, P. A.; Ridealgh, J.; Rosseinsky, M. J. Atomic layer deposition of germanium-doped zinc oxide films with tuneable ultraviolet emission. *J. Mater. Chem.* **2012**, *22* (25), 12824–12829.
- (36) Park, B. E.; Lee, Y.; Oh, I. K.; Noh, W.; Gatineau, S.; Kim, H. Structural and electrical properties of Ge-doped ZrO₂ thin films grown by atomic layer deposition for high-k dielectrics. *J. Mater. Sci.* **2018**, *53*, 15237–15245.
- (37) Jung, J. S.; Kim, D. H.; Shin, J. H.; Kang, J. G. Atomic Layer Deposition of GeO₂ Thin Films on Si (100) using Ge (N, N'-R, R-en)(NMe₂)₂ (Where R= Isopropyl and t-Butyl) Precursors. *Bull. Korean Chem. Soc.* **2015**, *36* (8), 1953–1954.
- (38) Yoon, C. M.; Oh, I. K.; Lee, Y.; Song, J. G.; Lee, S. J.; Myoung, J. M.; Kim, H. G.; Moon, H. S.; Shong, B.; Lee, H. B.; Kim, H. Water-erasable memory device for security applications prepared by the atomic layer deposition of GeO₂. *Chem. Mater.* **2018**, *30* (3), 830–840.
- (39) Larsson, F.; Keller, J.; Primetzhofer, D.; Riekehr, L.; Edoff, M.; Törndahl, T. Atomic layer deposition of amorphous tin-gallium oxide films. *J. Vac. Sci. Technol., A* **2019**, *37* (3), No. 030906.
- (40) Hall, L. H.; Bardeen, J.; Blatt, F. J. Infrared absorption spectrum of germanium. *Phys. Rev.* **1954**, *95* (2), 559–560.
- (41) Keller, J.; Sopiha, K. V.; Stolt, O.; Stolt, L.; Persson, C.; Scragg, J. J.; Törndahl, T.; Edoff, M. Wide-gap (Ag, Cu)(In, Ga) Se₂ solar cells with different buffer materials—A path to a better heterojunction. *Prog. Photovoltaics* **2020**, *28* (4), 237–250.
- (42) Yamashita, Y.; Takayanagi, K.; Gotoh, K.; Toko, K.; Usami, N.; Suemasu, T. Zn_{1-x}Ge_xO_y Passivating Interlayers for BaSi₂ Thin-Film Solar Cells. *ACS Appl. Mater. Interfaces* **2022**, *14* (11), 13828–13835.
- (43) Niemegeers, A.; Burgelman, M.; Herberholz, R.; Rau, U.; Hariskos, D.; Schock, H. W. Model for electronic transport in Cu (In, Ga) Se₂ solar cells. *Prog. Photovoltaics* **1998**, *6* (6), 407–421.
- (44) Minemoto, T.; Matsui, T.; Takakura, H.; Hamakawa, Y.; Negami, T.; Hashimoto, Y.; Uenoyama, T.; Kitagawa, M. Theoretical analysis of the effect of conduction band offset of window/CIS layers on performance of CIS solar cells using device simulation. *Sol. Energy Mater. Sol. Cells* **2001**, *67* (1–4), 83–88.
- (45) Gloeckler, M.; Sites, J. R. Efficiency limitations for wide-bandgap chalcopyrite solar cells. *Thin Solid Films* **2005**, *480*–481, 241–245.
- (46) Kuwahata, Y.; Minemoto, T. Impact of Zn_{1-x}MgxO: Al transparent electrode for buffer-less Cu (In, Ga) Se₂ solar cells. *Renewable Energy* **2014**, *65*, 113–116.
- (47) Chantana, J.; Kawano, Y.; Mavlonov, A.; Minemoto, T. Total band alignment in theoretical and experimental aspects for enhanced performance of flexible and Cd-free Cu (In, Ga)(S, Se) 2 solar cell fabricated by all-dry process. *Prog. Photovoltaics* **2023**, *31* (2), 161–172.
- (48) Cho, D. H.; Lee, W. J.; Kim, M. E.; Kim, K.; Yun, J. H.; Chung, Y. D. Reactively sputtered Zn (O, S) buffer layers for controlling band alignment of Cu (In, Ga) Se₂ thin-film solar cell interface. *J. Alloys Compd.* **2020**, *842*, No. 155986.
- (49) Sharbati, S.; Sites, J. R. Impact of the band offset for n-Zn (O, S)/p-Cu (In, Ga) Se₂ solar cells. *IEEE J. Photovoltaics* **2014**, *4* (2), 697–702.
- (50) Kobayashi, T.; Kumazawa, T.; Kao, Z. J.; Nakada, T. Cu (In, Ga) Se₂ thin film solar cells with a combined ALD-Zn (O, S) buffer and MOCVD-ZnO: B window layers. *Sol. Energy Mater. Sol. Cells* **2013**, *119*, 129–133.
- (51) Khatri, I.; Shudo, K.; Matsuura, J.; Sugiyama, M.; Nakada, T. Impact of heat-light soaking on potassium fluoride treated CIGS solar cells with CdS buffer layer. *Prog. Photovoltaics* **2018**, *26* (3), 171–178.
- (52) Shin, S. S.; Kim, K.; Yoo, J.; Kim, J. H.; Ahn, S.; Cho, A.; Kim, D.; Jo, Y.; Jeong, I.; Shin, D.; Cho, J. S.; et al. Heterojunction interface passivation strategy for Cu (In_{1-x}, Ga_x) Se₂ solar cell with nano-level engineering of Zn-based buffer structure via atomic layer deposition method. *Sol. Energy Mater. Sol. Cells* **2021**, *224*, No. 111010.
- (53) Nakada, T.; Kunioka, A. Direct evidence of Cd diffusion into Cu (In, Ga) Se 2 thin films during chemical-bath deposition process of CdS films. *Appl. Phys. Lett.* **1999**, *74* (17), 2444–2446.
- (54) Nakada, T.; Kobayashi, T.; Kumazawa, T.; Yamaguchi, H. Impacts of post-treatments on cell performance of CIGS solar cells with Zn-compound buffer layers. *IEEE J. Photovoltaics* **2013**, *3* (1), 461–466.
- (55) Takeshi Sugiyama, T. S.; Chaisitsak, S. C.; Yamada, A. Y.; Konagai, M. K.; Kudriavtsev, Y. K.; Godines, A. G.; Villegas, A. V.; Asomoza, R. A. Formation of pn homojunction in Cu (InGa) Se₂ thin film solar cells by Zn doping. *Jpn. J. Appl. Phys.* **2000**, *39* (8R), 4816.
- (56) Cui, X.; Sun, K.; Huang, J.; Yun, J. S.; Lee, C. Y.; Yan, C.; Sun, H.; Zhang, Y.; Xue, C.; Eder, K.; Yang, L.; et al. Cd-Free Cu 2 ZnSnS 4 solar cell with an efficiency greater than 10% enabled by Al 2 O 3 passivation layers. *Energy Environ. Sci.* **2019**, *12* (9), 2751–2764.
- (57) Ueda, S. T.; Kwak, I.; Abelson, A.; Wolf, S.; Qian, C.; Law, M.; Kummel, A. C. Electronic passivation of PbSe quantum dot solids by

trimethylaluminum vapor dosing. *Appl. Surf. Sci.* **2020**, *513*, No. 145812.

(58) Zywotko, D. R.; George, S. M. Thermal atomic layer etching of ZnO by a “Conversion-Etch” mechanism using sequential exposures of hydrogen fluoride and trimethylaluminum. *Chem. Mater.* **2017**, *29* (3), 1183–1191.

(59) Yu, X.; Yan, H.; Peng, Q. Reaction Temperature and Partial Pressure Induced Etching of Methylammonium Lead Iodide Perovskite by Trimethylaluminum. *Langmuir* **2019**, *35* (20), 6522–6531.

(60) Chantana, J.; Kawano, Y.; Nishimura, T.; Kimoto, Y.; Kato, T.; Sugimoto, H.; Minemoto, T. Transparent electrode and buffer layer combination for reducing carrier recombination and optical loss realizing over a 22%-efficient Cd-free alkaline-treated Cu (In, Ga)(S, Se) 2 solar cell by the all-dry process. *ACS Appl. Mater. Interfaces* **2020**, *12* (19), 22298–22307.

(61) Nakamura, M.; Yamaguchi, K.; Kimoto, Y.; Yasaki, Y.; Kato, T.; Sugimoto, H. Cd-free Cu (In, Ga)(Se, S) 2 thin-film solar cell with record efficiency of 23.35%. *IEEE J. Photovoltaics* **2019**, *9* (6), 1863–1867.

(62) Yang, J.; Siempelkamp, B. D.; Mosconi, E.; De Angelis, F.; Kelly, T. L. Origin of the thermal instability in CH₃NH₃PbI₃ thin films deposited on ZnO. *Chem. Mater.* **2015**, *27* (12), 4229–4236.

(63) Park, H.; Jeong, S.; Kim, E.; Shin, S.; Shin, H. Hole-Transporting Vanadium-Containing Oxide (V₂O_{5-x}) Interlayers Enhance Stability of α -FAPbI₃-Based Perovskite Solar Cells (~23%). *ACS Appl. Mater. Interfaces* **2022**, *14* (37), 42007–42017.